The Astronomical Journal, 169:53 (14pp), 2025 January https://doi.org/10.3847/1538-3881/ad93a2

The TANDEM Project as a Pilot Case for Wide-field Telescope Arrays

A. Buzzoni, A. Carbognani, R. Di Luca, E. Diolaiti, R. Gualandi, A. Semola, G. M. Stirpe, F. Bonoli, I. Bruni, F. Cortecchia, I. Foppiani, S. Galleti, M. Lombini, and L. Schreiber
INAF-OAS Osservatorio di Astrofisica e Scienza dello Spazio, Via P. Gobetti 93/3, I-40129 Bologna, Italy; alberto.buzzoni@inaf.it
Received 2024 August 07; revised 2024 November 04; accepted 2024 November 15; published 2024 December 27

Abstract

We give here an account of the Telescope Array eNabling DEbris Monitoring (TANDEM) project, an innovative concept aimed at flanking, on a shared piggyback mount, the main G. D. Cassini 152 cm $f/8$ telescope at the INAF-OAS observing premises in Loiano, Italy. The system is especially intended for space situational awareness activities related to the study of asteroids and comets and on the astrodynamical characterization of circumterrestrial space debris and artificial satellites. TANDEM consists of a combination of four customized and independently steerable 35 cm $f/3$ Newtonian telescopes, each equipped with a Moravian C4-16000 camera, observing through the BVR_cI_c filters of the Johnson–Cousins system. The camera carries on board a GSense 4040 (4096×4096 pixels) monochrome CMOS detector with an electronic shutter and a 9 μm pixel size. A corrected field of view of $2^\circ \times 2^\circ$ is offered by each telescope, though quite special pointing capabilities and observing modes are available for the telescope array, such as to cover up to 16 deg^2 across sparse celestial fields, each up to 20° in separation. While especially conceived for observing activities in the framework of the European Consortium for Space Surveillance and Tracking, TANDEM may also find additional applications in a more direct astronomical context, as we briefly outline along this review.

Unified Astronomy Thesaurus concepts: Telescopes (1689); Wide-field telescopes (1800); Telescope properties (2350); Focal ratio (2353); Sky surveys (1464)

1. Introduction

Recent (and still ongoing) advances in digital detector technology have raised again the interest of astronomers and other sky watchers for wide-field capabilities in ground-based telescopes. A change of paradigm has to be reported, in this sense, in the observational approach during the last decades, where wide-field performances were originally the rule for (now small) telescopes up to the 1970s, favored by the use of big (though relatively "blind") photographic plates as detectors.

With the advent of more sensitive CCDs, the field of view (FOV) of those same telescopes shrunk dramatically as only a small fraction of the corrected image at the focus could be intercepted by the then-small electronic chips (see I. Furenlid 1984, for a comparative discussion). As a consequence, in the following decades, deep-sky observations remained (forcedly) prevalent in wide-field astronomy.

Only in more recent years this process has been reversing, as digital imaging now takes advantage of (much) bigger solid-state detectors, with an increasing role of CMOS technology accompanying (and often replacing) the CCD imagers (see, e.g., B. Burke et al. 2005; A. Hoffman et al. 2005; N. Waltham 2010; S. Karpov et al. 2020, for up-to-date informative reviews on these technologies). In addition, digital techniques massively affected the way optical parts are manufactured and assembled (J. Dorißen et al. 2022 provided an instructive discussion), thus making wide-field telescopes of the new generation "faster" and optically more elaborate (the LSST project is an outstanding milestone in this regard; J. A. Tyson 2002; Ž. Ivezić et al. 2019).

Surveys of celestial objects and transient events across wide portions of the sky span a range of cases, not only of strict astronomical interest but also including all those activities more generally related to space situational awareness (SSA) in the different space contexts. A thoughtful screening of the solar system in search for incoming interstellar intruders, or new asteroids and comets, may therefore flank the comprehensive census of stars within our own Galaxy, or the study of galaxy clusters at cosmological distances. A quick reaction and a wide field under survey are also mandatory for those extemporary events possibly related to gravitational waves (GWs) and gamma-ray bursts (GRBs), somewhere in the Universe.

Besides astronomical topics, space surveillance and tracking (SST), may also be of special appeal, in this regard, for a large audience among military, commercial, and scientific communities, as the surging population of anthropic objects (satellites and space debris) in the space environment surrounding Earth now needs to be actively assessed for its potentially pervasive impact on other human activities (J. Blake 2022; A. Lawrence et al. 2022; A. Mariappan & J. L. Crassidis 2023), not least the disruptive consequences on ground-based and low-orbit astronomical observations (see, e.g., O. R. Hainaut & A. P. Williams 2020; S. M. Lawler et al. 2022, for a thoughtful analysis).

Though so different, both the deep-space and circumterrestrial explorations rely in fact on the same strategy: enhanced collecting area and a wide FOV are the two ultimate requirements for our telescopes to push target detection and positional tag at the faintest magnitude levels. However, when high angular resolution is not a leading issue against wide-field capabilities, we have shown (A. Buzzoni 2024b) that a suitable assembly of small telescopes to synthesize the full collecting area of a larger monolithic instrument may provide a basically equivalent and cost-effective solution.

As an effort to effectively implement this scheme in the framework of best value-for-money technical solutions, in this paper we want to give an account of the Telescope Array eNabling DEbris Monitoring (TANDEM) project, which led to a telescope array for SST and astronomical use, recently set in operation at the INAF-OAS observing premises in Loiano (Bologna), Italy. In the following, Section 2 sets the context and the motivation background that led to the conception of TANDEM. The story of this exciting endeavor is then briefly outlined in Section 3, detailing the technical and optical properties of the telescope combination in Sections 3.1 and 3.2. Quite special pointing capabilities are available for the TANDEM telescopes, giving the instrument a range of observing modes, as outlined in Section 3.3. The optical characterization is discussed in Section 3.4, while all the relevant features of the project, including a final discussion, are given in Section 4, in view of the envisaged scientific applications of the instrument.

2. Telescope Array versus Monolithic Design: Setting the Context

In principle, a monolithic telescope[1] (of full diameter D), is therefore a diffraction-limited instrument, where angular details can be appreciated depending on the observing wavelength (λ), within an inherent resolution of the order of (λ/D) radians (e.g., D. J. Schroeder 1987). However, as far as ground-based telescopes are concerned, even for small decimeter-size diameters, it is easy to verify that the blurring effect of atmospheric turbulence always greatly exceeds the nominal diffraction pattern of the optics (e.g., F. Roddier 1981), thus making our telescope's resolving power actually seeing (not diffraction) limited. Of course, more elaborate (and expensive) adaptive-optics solutions could greatly alleviate the situation, but always at the cost of drastically reducing the FOV capabilities of our instrument.

For this reason, if angular resolution is not of primary concern for our observations against wide-field requirements, then one could better decide to waive optical coherence just in favor of a big "synthetic" telescope such as an array of smaller (independent) instruments. A. Buzzoni (2024b) has shown that this strategy may have a substantial financial edge once (i) a wide FOV is of interest for our research, and (ii) a decoupling may be accepted between resolving power and magnitude limit in target detection, favoring the latter option.

A plain (yet decisive) technical argument in favor of a telescope-array solution is that a factor of $\sqrt{N}$ reduced $f/$number can be achieved when combining N (similar) telescopes, each of diameter $d_{\rm array}$ and focal length $F_{\rm array}$, to synthesize an equivalent monolithic diameter $D_{mono} = \sqrt{N} d_{array}$ and $f_{\rm mono} = (F_{\rm array}/D_{\rm mono}) = f_{\rm array}/\sqrt{N}$ (on a similar line, see also R. G. Abraham & P. G. van Dokkum 2014, for a discussion of this important point in the framework of the Dragonfly project). This would easily match our observing requirements, as a larger FOV would in general benefit from a shorter telescope focal length (i.e., a "fast" $f/$number), while a fainter magnitude limit would be reached by a larger diameter of the "synthetic" primary mirror.

As far as market figures for cost off-the-shelf telescopes are considered, a key relationship (A. Buzzoni 2024b) links cost (C) with telescope diameter and $f/$number, namely

$$C \propto D^{2.10\pm0.24} f^{-0.70\pm0.08}. \tag{1}$$

As cost scales more than linearly with the collecting area (D^2), by itself this makes a telescope array marginally more convenient to reach a given size for the primary mirror with respect to its equivalent monolithic case. In addition, and somewhat more relevant, as less demanding $f/$numbers are required for the array components ($f_{\rm array}$), compared with the synthetic output ($f_{\rm mono}$), then further savings can be envisaged according to Equation (1). Allover, the full array cost ($C_{\rm array}$) compared to an equivalent monolithic case with the same total collecting area ($C_{\rm mono}$) results

$$\left(\frac{C_{\rm array}}{C_{\rm mono}}\right) = N^{-0.40\pm0.16}. \tag{2}$$

For a four-telescope combination, this makes a 43% saving. Clearly, a more complete budget breakdown analysis should also consider that additional CCD/CMOS detectors are required by the telescope array. Especially in the case of small telescopes of decimeter class, this item could drastically impact on the total cost. By considering that one detector must be acquired in any case, we have that the per-item cost ($c_{\rm CCD}$) of the additional $N-1$ detectors is

$$c_{\rm CCD} \leqslant N\left(\frac{N^{0.40\pm0.16} - 1}{N - 1}\right) c_{\rm array}, \tag{3}$$

where is the cost one single telescope (optical tube assembly; OTA) of the array ensemble. Note that for a four-telescope array, $c_{\rm CCD} \simeq c_{\rm array}$, that is each telescope could still be conveniently equipped with a CCD/CMOS camera of OTA comparable cost.

3. The Pathway to TANDEM

The previous arguments set the motivational background to further investigate the concept of a telescope combination to flank the main G. D. Cassini 152 cm $f/8$ telescope at the INAF-OAS observing premises in Loiano, Italy. The original intent aimed at expanding and completing the overall observing capabilities of the instrument, especially focused on already established SSA activities related to the study of asteroids and comets (A. Carbognani & A. Buzzoni 2020; A. Carbognani et al. 2021; M. Fulle et al. 2022) and on the astrodynamical characterization of circumterrestrial space debris and artificial satellites (A. Buzzoni et al. 2016, 2019a, 2019b; M. Micheli et al. 2018b; E. M. Alessi et al. 2021; J. Daquin et al. 2021; A. Di Cecco et al. 2023).

3.1. Final Concept and Instrument Timeline

The TANDEM project began to take shape around 2015, as a valuable proxy to the ongoing effort to recover the original wide-field capability of the Cassini telescope (namely, a 72′ corrected FOV projected on a 25 cm wide spot on the image plane at the $f/8$ Cassegrain focus), only barely exploited until then due to the limited CCD size of the available instrument BFOSC.

Any obvious solution, either by relying on a composite CCD/CMOS mosaic, or by reducing Cassini's $f/3$ prime focus such as to project the full FOV on a medium format

[1] With "monolithic" we intend all those telescopes consisting either of a single dish or a segmented primary mirror, such as to lead to an image at the focus by fully preserving the optical coherence of the incoming wave front, i.e., both intensity and phase angle.

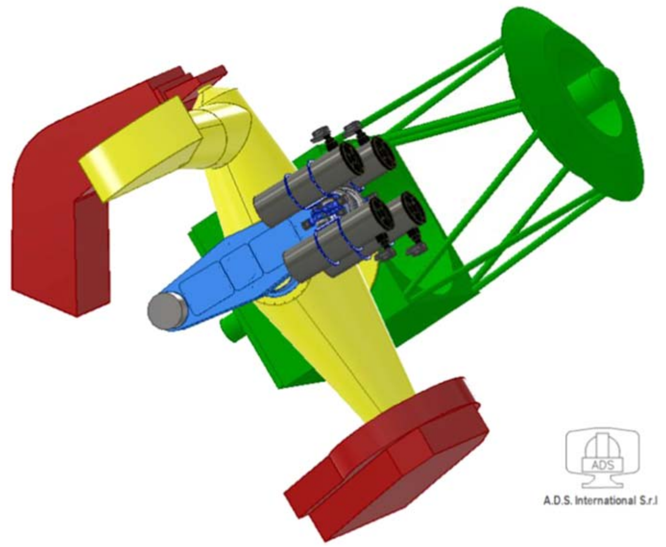

Figure 1. The ADS concept for TANDEM, as approved for final assembly in summer 2022. Note in the sketch the four telescopes (in black) mounted on a rotating arm (in blue) anchored orthogonally to the Cassini (in green) polar axis (in yellow).

CCD/CMOS chip, promptly proved to be unattainable both for financial and technological constraints. These overwhelming limitations led eventually to a drastic change of paradigm such as to rethink a "new Cassini" concept as a composite instrument, consisting in fact of an assembly of smaller telescopes to flank the main sensor on the same equatorial mount as a sort of megabinoculars.

A challenging "fast" focal ratio of $f/3$ for the supplementary telescopes, as for Cassini's primary mirror, and arguments of structural symmetry of the combined design, suggested to accompany the main instrument with a service array of four smaller telescopes, each in the 30–40 cm aperture range. Though not reaching the full Cassini aperture, when combined, these telescopes could conveniently match the collecting area of a monolithic mirror of 60–80 cm in diameter sporting an even "faster" focal ratio of $f/1.5$. Most importantly, as a major added value of this choice, this new "synthetic" telescope could in principle supply an even wider FOV, up to 2°–$2\overset{\circ}{.}5$ across the sky, compared with the $13' \times 13'$ FOV currently offered by the 152 cm telescope equipped with the BFOSC camera.

With these milestones in mind, late in 2018 a detailed feasibility study was commissioned to the NPC Spacemind enterprise of Imola (Italy), in order to carefully assess also the structural constraints for safely anchoring the (then-named) new optomechanical system at the Cassini mounting. Different concepts were explored for a piggyback mounting fork at the main polar axis. Following an official call for tenders, in spring 2022, TANDEM realization was assigned to ADS International, based in Annone Brianza, Italy.

The final concept of the instrument (with a color-coded rendering) is displayed in Figure 1. According to the design, TANDEM had to be anchored at the Cassini's decl. axis flange on top of a rotating arm (shown in blue in Figure 1), the latter for the twofold scope of overcoming the counterweight obstruction when observing at polar decl. and allowing the telescope combination to account for the possible 180° pointing switch of Cassini, when maneuvering from the "face-east" to "face-west" configurations.

A successful factory acceptance test of the assembled instrument, in 2023 June, made TANDEM ready to be eventually moved to Loiano and successfully installed at the Cassini original mount (Figure 2). Immediately after installation, first light was obtained in the night of 2023 June 28 (see Figure 3) with an iconic image of the Moon taken in blue light with the shortest exposure time allowed by the electronic shutter of the CMOS, namely just 0.02 ms.

According to the following discussion, a synoptic summary of the Cassini + TANDEM system is reported in Table A1 of the Appendix.

3.2. Optical Design

TANDEM consists of a battery of four customized AG14 $f/3$ Newtonian telescopes, built by ORION Ltd. (UK), each with aperture of 35 cm (see Figure 4). Each telescope is equipped with a Moravian C4-16000 camera carrying a motorized and remotely controlled filter wheel.

The camera carries on board a front-illuminated Grade 1 GSense 4040 (4096 × 4096 pixels) monochrome CMOS with an electronic shutter. The CMOS pixel technology includes a microlens array (CMT), while the chip is sealed with D263T lids and an antireflective coating on both sides. The detector is cooled down to 35 °C below ambient by means of a thermoelectric (Peltier) module. A 9 μm pixel size provides 17 Mpixel imagery at a 16 bit counting depth across a $2^\circ \times 2^\circ$ wide FOV fully corrected for astigmatism and coma aberration via a 4″ Wynne corrector. The latter was ad hoc manufactured by Tecnottica Consonni srl, in Calco (Lecco, Italy), based on our own original optical concept. The plate scale (PS) at CMOS is $1\overset{''}{.}75$ pixel^{-1}.

In addition to a "clear" (i.e., no filter) observing slot, a set of four BVR_cI_c filters (50 mm in diameter) is mounted on the five positions of each wheel, closely matching the Johnson–Cousins photometric system (H. L. Johnson 1966; A. W. J. Cousins 1976), as summarized in Table 1. The spectral transmission curves of the GSense 4040 detector and the filters are shown in Figure 5.

3.2.1. Image Quality

Given the relatively small telescope aperture, a Newtonian optical design was eventually the chosen solution for the TANDEM telescopes. The latter allows in fact a more convenient match with the focus devices (i.e., CMOS camera, motorized filter wheel, and the additional lense train for the field corrector), which on the contrary would lead to a massive obstruction of the primary mirror in case of a prime-focus implementation, as in standard astrograph instruments.

A delicate trade-off had to be considered, however, between size and position of the secondary mirror and the optical design of the Wynne corrector in order to minimize any vignetting effect of the whole optical system. The two panels of Figure 6 give a sketch of the relevant parameters in the optical problem we had to optimize. Disregarding for a moment the Wynne corrector, in the case of straight on-axis paraxial imagery (left panel of the figure), the size of the secondary mirror[2] (d) directly depends on the intercepting distance from the primary mirror (D) to extract the focus outside the optical tube. If a distance ($F - X$) from the primary mirror is chosen, this simple

[2] In any case, the secondary mirror is elliptical. Throughout our discussion, its size refers to the full minor axis of the ellipse.

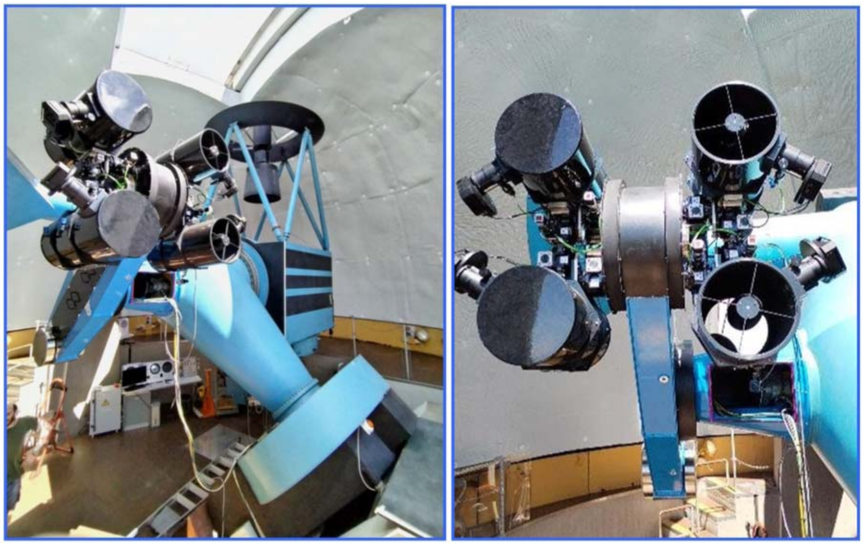

Figure 2. Two views of the TANDEM telescope array, on top of its rotating arm, in a piggyback mounting at the decl. axis flange of the Cassini main telescope (behind in the left picture). TANDEM telescopes share Cassini's polar axis maneuvering, while moving the combination independently in decl. In addition, each of the telescopes is allowed a supplementary and independent steering by $\pm 10°$ around the common pointing direction (both R.A. and decl.) by means of individual tilt/spin actuators on board (visible in the right picture).

Figure 3. The "first light" of TANDEM, just after the preliminary focusing operations on 2023 June 28. A spectacular B-band image of the waxing gibbous Moon is taken with the shortest exposure time allowed by the electronic shutter on board the CMOS, namely just 0.02 ms.

proportion holds

$$d: X = D: F, \tag{4}$$

providing that $(X - D/2) \geqslant 0$ if we want the focus plane (F) external to the optical tube.

Of course, any CMOS detector of size c (full diagonal across the chip) the focus F will intercept a wider field, so that a slightly larger secondary mirror (d'), compared to the simple on-axis paraxial case, is required to collect the full optical beam coming from the primary mirror. For this case, it is useful to rely on a fictitious focus (F'), as in the right panel of Figure 6, in excess of an x' distance with respect to the physical focus of the system, so that $F' = F + x'$. Again, in this case a straightforward proportional relationship must hold such as

$$c: x' = d': (X + x') = D: F'. \tag{5}$$

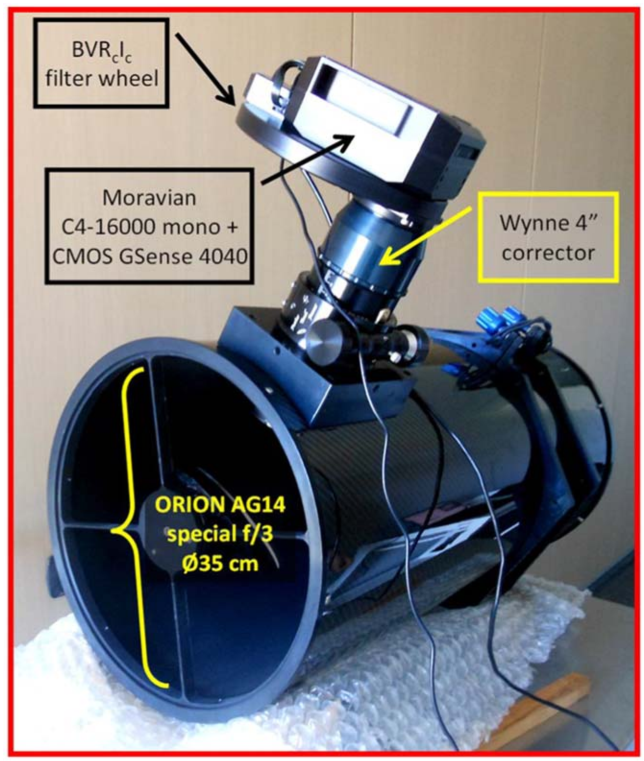

Figure 4. The optical design of the TANDEM telescopes. Each instrument is a customized ORION AG14 telescope with a 35 cm aperture diameter and Newtonian design, carried to a focal ratio $f/3$ and coupled with an ad hoc 4″ Wynne field corrector. Imagery is provided through a Moravian C4-16000 camera mounting a Johnson–Cousins $BVRI$ filter wheel and a CMOS GSense 4040 (4096×4096 pixels with 9 μm pixel size).

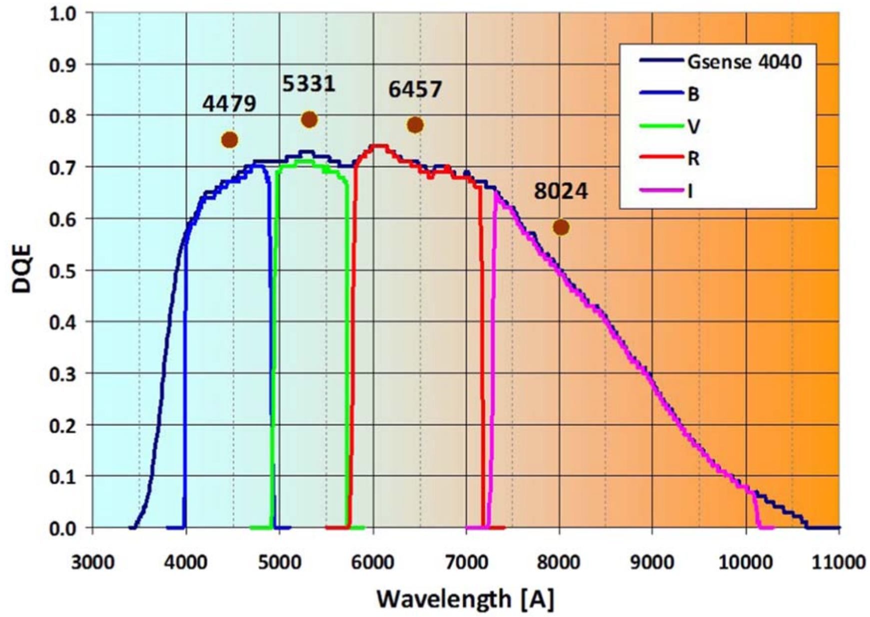

Figure 5. The TANDEM photometric system includes a set of four BVR_cI_c filters. Effective wavelengths (dots and labels in the plot) fairly well reproduce the Johnson–Cousins system. As a common feature, note that the I_c band is in fact mainly constrained by the CMOS spectral transmission.

Table 1
The TANDEM BVR_cI_c Photometric System According to the Johnson–Cousins Standard

Filter	$\lambda_{\rm eff}$ (Å)	Full-width Passband (Å)	Note
C (GSense 4040)	6355	3700	[a]
B	4479	930	…
V	5331	800	…
R_c	6457	1400	…
I_c	8024	1340	[a]

Note.
[a] For these cases, bandwidth is computed according to the detector quantum efficiency, DQE, as $\mathrm{FW} = 2.35\left\{\frac{\Sigma[(\lambda-\lambda_{\rm eff})^2 \mathrm{DQE}(\lambda)]}{\Sigma \mathrm{DQE}(\lambda)}\right\}^{1/2}$.

By combining the first and third terms of the proportion, a condition for F' can be set such as

$$F' = \frac{F}{(1 - c/D)}. \tag{6}$$

This relationship helps constrain the enhanced size of the secondary mirror, compared to the paraxial size, via the middle term of Equation (5)

$$\frac{d'}{(X + F' - F)} = \frac{D}{F'}, \tag{7}$$

by replacing $X = Fd/D$ from Equation (4). With a little algebra we finally have

$$d' = d\left(1 - \frac{c}{D}\right) + c. \tag{8}$$

As expected, the wide-field relation approaches the paraxial case as a limit with decreasing the chip size (c).

On similar arguments, a supplementary analysis is also needed to characterize the Wynne field corrector. In particular, as shown in the right panel of Figure 6, the first (field) lens of the correcting train must be placed at a distance $(X - W) \geqslant D/2$ from the secondary mirror to avoid any intrusion in the optical tube and obstruction of the incoming light.[3] As for Equation (5), a geometrical proportion holds, such as

$$c: x' = L_1: (W + x') = D: F'. \tag{9}$$

Similarly to Equation (8), this eventually leads to an inherent structural relationship for the corrector, as a function of the telescope f/number and the chip dimension

$$\frac{L_1}{W} = \frac{1}{f}\left(1 - \frac{c}{D}\right) + c. \tag{10}$$

Note that the length W directly depends on the chosen size for L_1. A smaller field lens will in general require a more compact (and usually more elaborate and expensive) corrector. Based on Equations (4), (8), and (10), we can set up a diagnostic diagram for the optical design of the TANDEM telescopes as in Figure 7.

In addition to optical arguments, mechanical constraints on the telescope barycenter and inertial momentum for efficient maneuvering of the whole system have to be considered for the final configuration of the telescopes. For instance, a reduced distance $(F - X)$ of the secondary mirror from the primary one would make the telescope more compact and faster to point, though at the cost of a larger optical obstruction of the entrance pupil and a more severe off-axis extrusion of the whole imager block (which, by the way, carries a substantial fraction of the system's full weight). Conversely, a smaller secondary mirror at increased distance would alleviate obstruction but at the cost of a more demanding (and likely costly) field corrector, now shorter and optically more elaborate.

[3] Note that this can be regarded as the "length" of the Wynne corrector assuming, for the illustrative scope of our discussion, the telescope focal length remains unaffected by the supplementary optics. Accordingly, the maximum length allowed to the field corrector is $W_{\max} = (X - D/2)$.

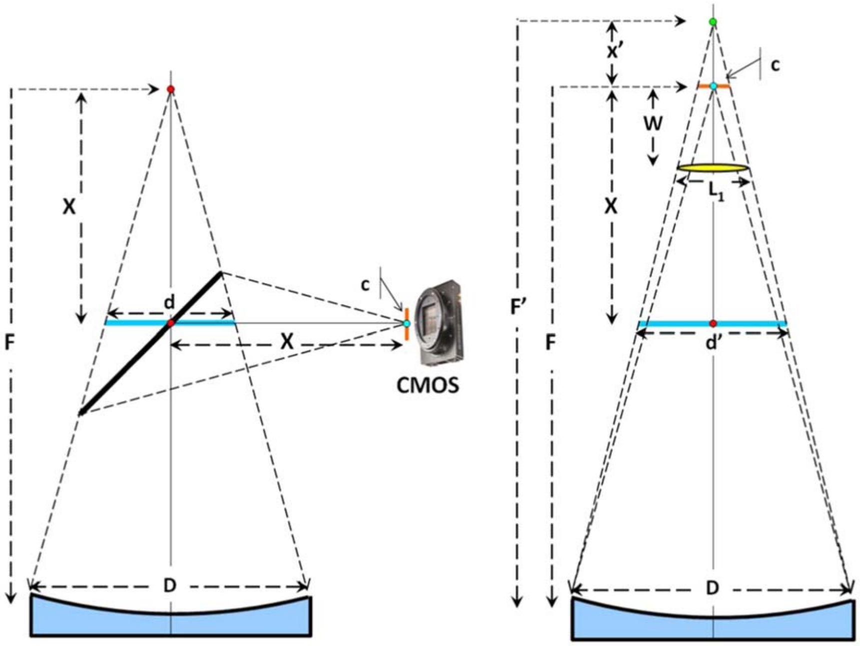

Figure 6. An illustrative sketch of the relevant parameters for TANDEM's optical design optimization. See text for a full discussion.

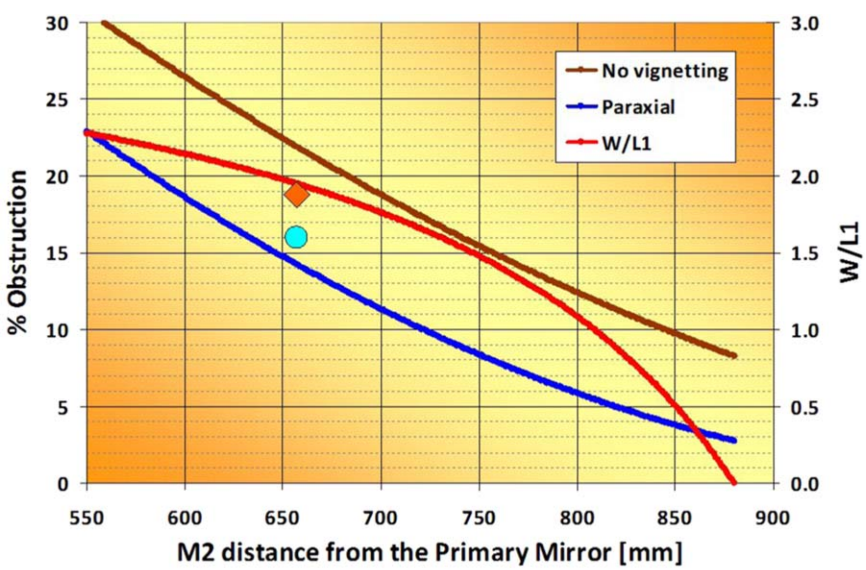

Figure 7. A diagnostic diagram for the optical design of the TANDEM telescopes. The 16% obstruction of the entrance pupil for the adopted size of the secondary mirror, placed at a distance $(F-X)=657$ mm from the primary mirror, is marked by the blue dot. It is compared with the expected obstruction for the size of the secondary mirror such as to intercept the paraxial optical beam only (blue curve) or the full FOV with no vignetting (brown curve). The nominal ratio W/L_1 for the Wynne corrector train is also displayed, according to Equation (10) (the red curve refers to the right scale on the plot), compared with the adopted figure for the telescopes (red diamond). The red curve has to be regarded as an upper limit to the optimal optical combinations. See text for a full discussion of these quantities.

The adopted solution for the TANDEM telescopes, also marked in Figure 7, eventually relied on a distance $(F-X)=657$ mm for the secondary mirror, by setting its size $d_{M2}=140$ mm. This induces a 16% reduction of the telescope collecting area. The adopted dimension oversizes the paraxial case (i.e., $d=131$ mm according to Equation (4)) but accepts however a little amount of vignetting (as $d_{M2}<d'=164$ mm, as from Equation (8)). This is shown in Figure 8, where we report the result of a direct assessment of the effect via a standard flat-fielding observing procedure. As expected, the central $1^\circ\times1^\circ$ region remains unaffected while a residual vignetting is evident across the outermost portion of the FOV, reducing the incoming signal by about 0.15 mag at the $2^\circ\times2^\circ$ edge of the frame.

3.2.2. Image Quality Optimization

A fast parabolic mirror, such as the primary mirror of the TANDEM instruments, is affected by significant field aberrations (e.g., astigmatism and coma) and a curved image surface at the focus. This evidently poses a problem with any standard detector and requires a supplementary optical train to suitably correct the wide FOV. The problem is a classical one and, for parabolic primary mirrors, it has been extensively studied by C. G. Wynne (1972a, 1972b, 1974) in a series of reference

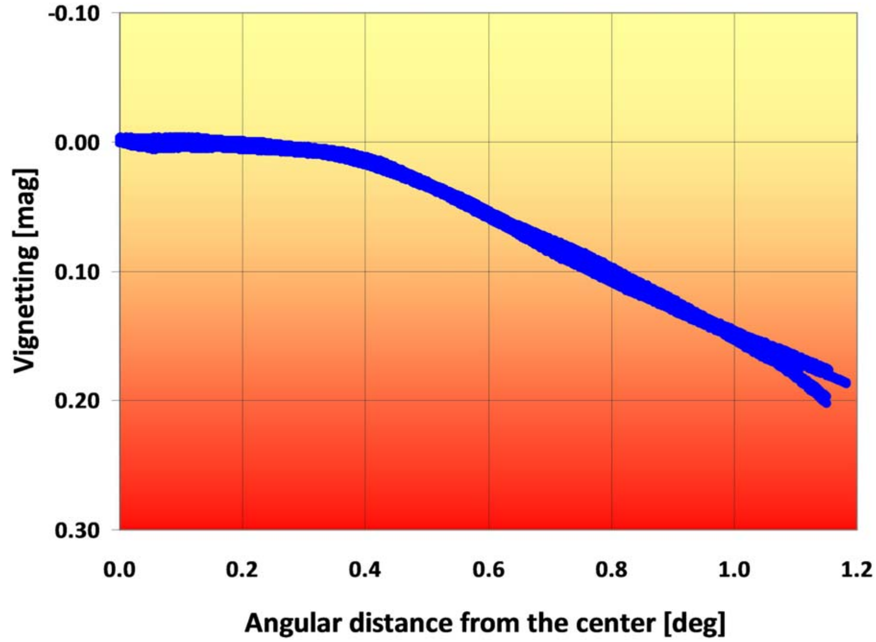

Figure 8. The superposed TANDEM radial profile of vignetting, as directly assessed from each of the four telescope's FOV. According to the adopted size of the secondary mirror we have that the central 1° × 1° region of the frame is virtually unvignetted while a residual effect of up to 0.15 mag appears at the 2° × 2° edge of the frame.

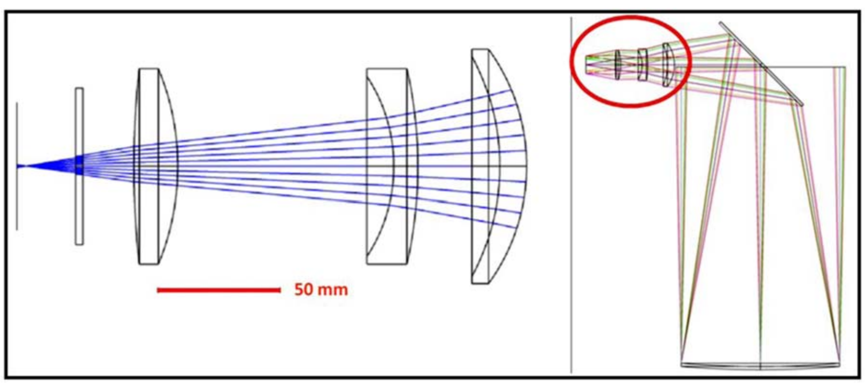

Figure 9. Left panel: the adopted optical design for the Wynne corrector on board the TANDEM telescopes. The optical train is placed just in front of the CMOS detector (and the filter wheel), and intercepts the incoming optical beam from the secondary mirror of the Newtonian system, as sketched in the right panel.

papers. Although evolved in many optical variants, the original Wynne corrector basically relies on a triplet of lenses with slightly positive–negative–positive optical power, as in Figure 9. Aside the primary task aimed at compensating the optical aberrations of the primary mirror, the corrector might also act as a focal reducer/extender, thus changing, if required, the f/number of the telescope.

For the TANDEM telescopes we simply relied on a classical three-lens configuration (see again Figure 9), carefully tuned to match the incoming optical beam from the telescope secondary mirror along the full 4000–9000 Å wavelength range and compensate the optical aberrations of the primary mirror, with a neutral impact on the final focal length of the system (thus maintaining the $f/3$ focal ratio). The design optimization was carried out with the Ansys Zemax OpticStudio optical design software package.[4] Each component of the triplet has been suitably coated against internal reflections.

The resulting image quality of the full optical system (primary and secondary mirrors, coupled with the Wynne correcting triplet) has been assessed through classical diagnostic plots, as summarized in Figure 10. The figure combines a multicolor spot diagram, as seen through the BVR_cI_c filters at increasing angular distance from the optical axis, together with the radial trend of the rms spot radius at the different wave bands.

Going by the CMOS pixel size, in both cases, it is confirmed that the TANDEM telescopes assure a nominal FWHM for point sources across the central 2° spot of the FOV fully comprised within 1 pixel. Of course, in order to obtain the real observing output of the telescopes, one has then to convolve with the seeing broadening and the mechanical tolerance in the optical system assembly. Allover, the preliminary on-sky tests confirm that the TANDEM telescopes sport a typical stellar FWHM about 2.0 pixel, or some $3\overset{\prime}{.}3$–$3\overset{\prime}{.}5$, on average, across the full imaged FOV.

3.3. Pointing Capabilities and Optimization

Due to its structural properties, TANDEM shares part of the Cassini pointing capabilities. In particular, the fixed anchoring

[4] Available at https://www.ansys.com/products/optics/ansys-zemax-opticstudio.

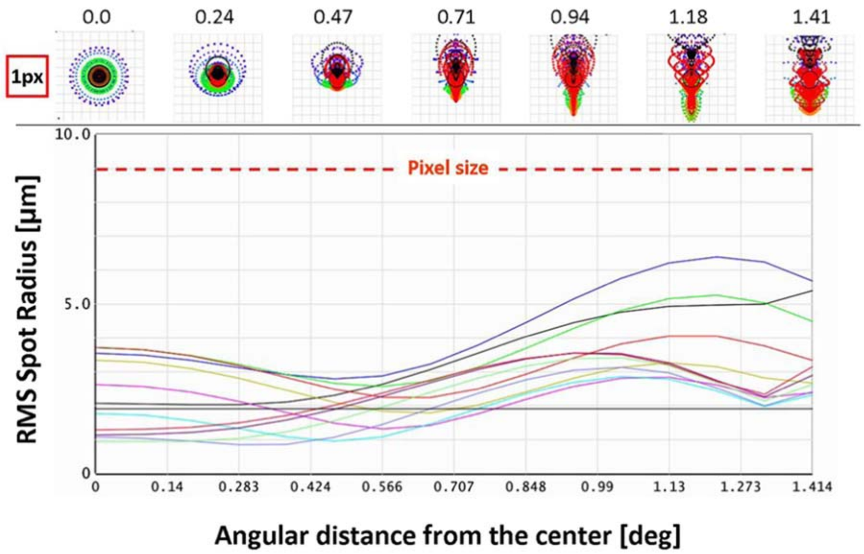

Figure 10. TANDEM telescopes' image quality diagnostics, according to Zemax OpticStudio modeling. The upper sequence displays a multiwavelength spot diagram at increasing radial distance (in degrees) from the optical axis, as labeled above each spot. Johnson–Cousins filters are color coded in the spots as B = blue, V = green, R_c = red, and I_c = violet. The pixel size is reported at the top left, as a reference. The lower plot displays the rms spot radius (in units of μm) along the radial distance from the CMOS center for a set of sampled wavelengths in the 4000–9000 Å range, as schematically color coded by the curves in the plot. The black curve refers to the polychromatic response, while the horizontal line at 1.91 μm is the diffraction limit set by the Airy disk. The 9 μm pixel size of the GSense 4040 CMOS is marked as a dashed red line, as labeled. The nominal figures do not take into account seeing broadening and mechanical tolerance in the optical system assembly.

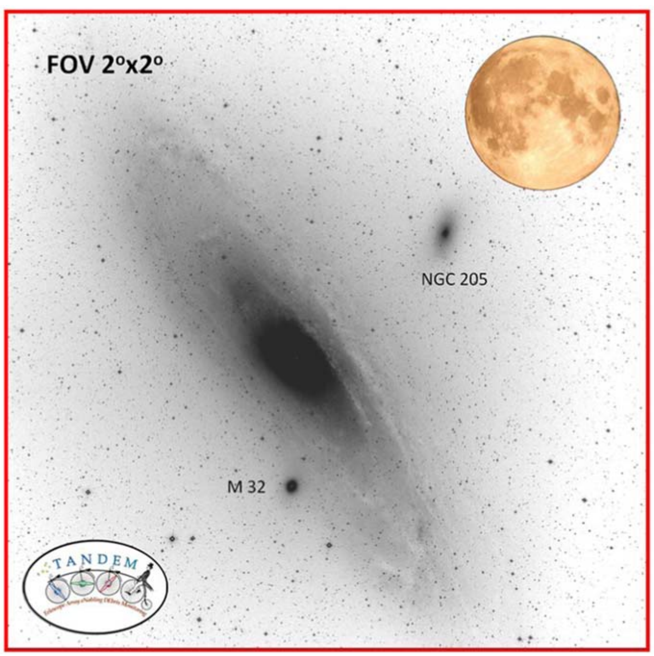

Figure 11. The covered FOV of TANDEM in "collimated" configuration, with the four telescopes pointing at the same $2^\circ \times 2^\circ$ field. The celestial region around the Andromeda galaxy, M31, is displayed as an illustrative reference, together with a full Moon sketch. Though with a smaller FOV, this configuration allows the observer to maximize TANDEM sensitivity, reaching a 0.75 mag deeper limit compared to imaging with a single telescope.

of the TANDEM steering arm at the Cassini decl.-axis flange makes the telescope combination share the hour angle (and correspondingly the celestial R.A.) with Cassini. On the contrary, decl. pointing is decoupled, as TANDEM can move the four telescopes according to each's own decl. axis, which is on board the steering arm and allows the telescope set to cover the full range from decl. of -30° to $+90^\circ$ on sky. In addition, and most importantly, one has to consider that each of the TANDEM telescopes is allowed a supplementary and independent steering by $\pm 10^\circ$ around the common pointing direction (both R.A. and decl.) by means of individual tilt/spin actuators on board.

This relevant characteristic allows the observer to trade-off angular and sensitivity performances. One can either use TANDEM at its best magnitude sensitivity by converging the four telescopes on the same $2^\circ \times 2^\circ$ FOV, as in Figure 11, such as to match a 70 cm $f/1.5$ monolithic telescope or, alternatively, fully exploit the wider angular coverage on sky by steering each telescope in a different direction such as to mosaic four adjacent fields, $4^\circ \times 4^\circ$ across, or simultaneously targeting four sparse fields up to 20° apart for up to 16 deg^2. A number of predefined pointing patterns is made available by the system (see Figure 12) and other user-defined configurations can, if required, be easily implemented.

In order to prevent the dome shutter to introduce any vignetting or definitely block the view of some of the telescopes, for the latter case the TANDEM control system will automatically reassign the telescopes to each field, such as to maintain a "convergent" pointing pattern across the dome shutter. An example is shown in Figure 13.

3.3.1. Control Software

Simultaneous operation of the four TANDEM telescopes is carried out by means of a dedicated control software. The observer can interact either manually or via a script for automatic data collection. In manual mode, the GUI provides the observer with a $20^\circ \times 20^\circ$ stellar map,[5] down to $V \sim +6$, centered on the nominal pointing of the telescope array, and locates on the map the color-coded individual position of each of the four instruments, according to any customized or preset pointing configuration, similar to Figure 12.

[5] The Yale Bright Star Catalog (D. Hoffleit & W. H. Warren 1987), available at http://tdc-www.harvard.edu/catalogs/index.html, is used for this task.

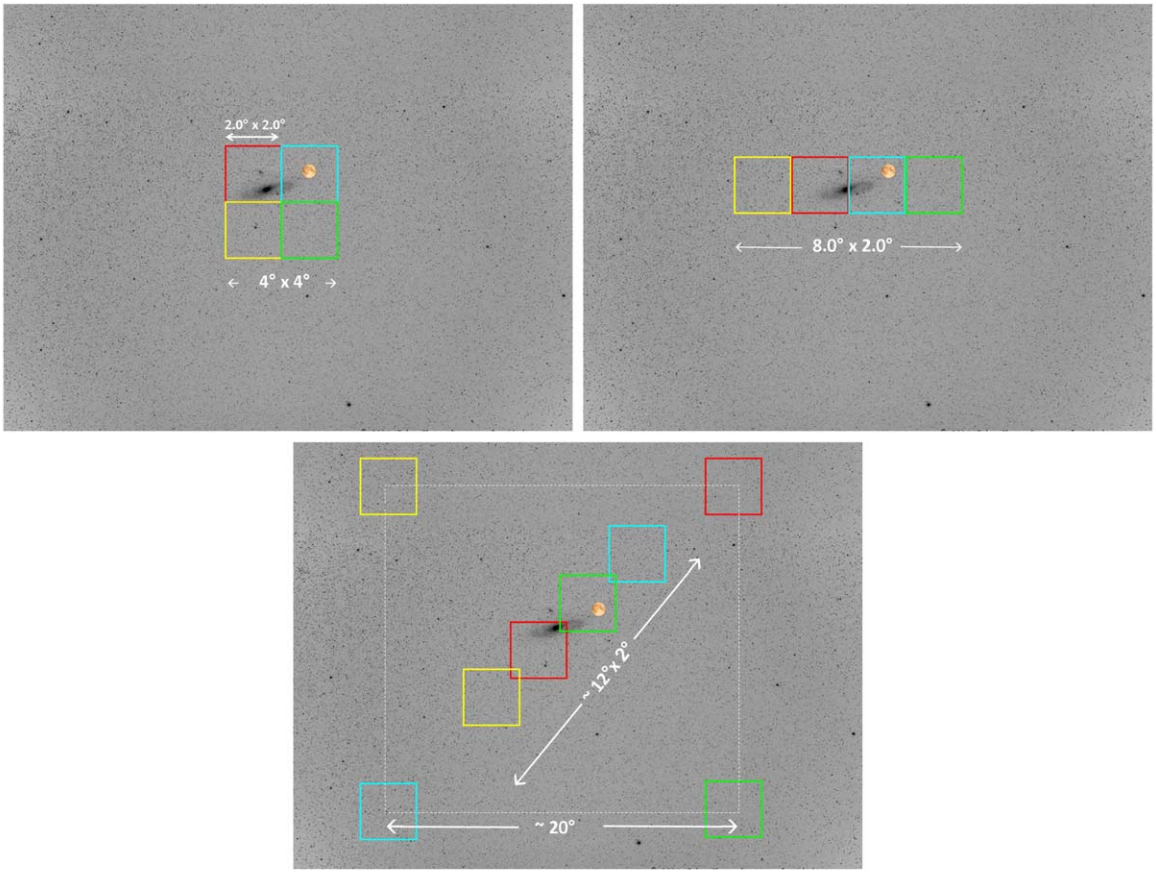

Figure 12. Some of the predefined pointing patterns for the four TANDEM telescopes (each marked with a different color). As a reference, the celestial region around the Andromeda galaxy, M31, has been displayed, together with a full Moon sketch. Note in particular, in the lower panel, two very extended "sparse-field" options, one along a diagonal direction spanning a $12^{\circ} \times 2^{\circ}$ FOV and the other consisting of four independent pointings each 20° apart.

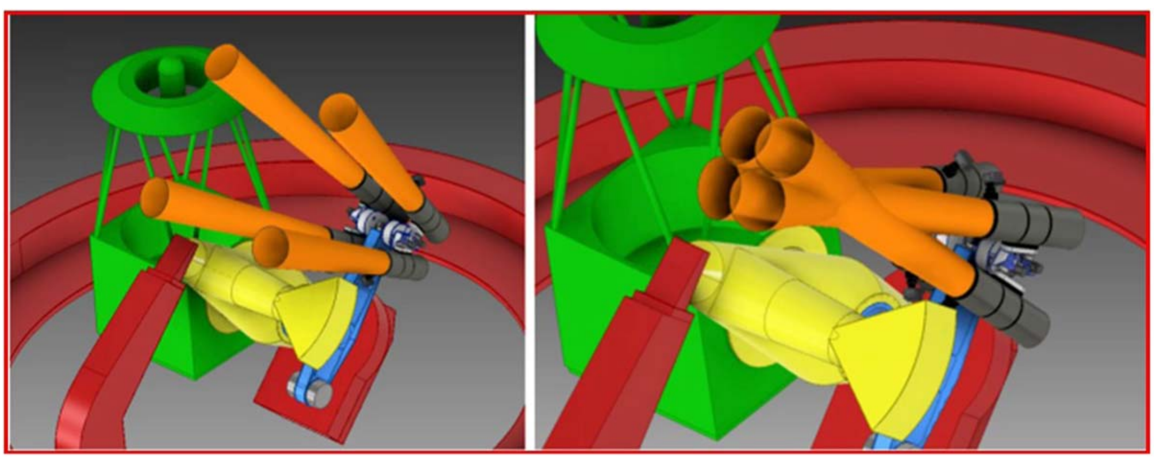

Figure 13. The same pointing is compared before (left) and after (right) TANDEM optimization. Note in the right panel that the four telescopes are automatically reassigned to each field such as to obtain a converging pointing pattern that minimizes the cross section through the dome shutter.

Of special interest for any SST activity, the control software takes in charge also TANDEM PC's clock synchronization via the network time protocol to the local global positioning system server in order to maintain the time tag of observations within an exquisite accuracy of a few milliseconds.

For each telescope, the exposure time and filter configuration can be set from the interface, together with the CMOS temperature and binning mode. A possible time delay between the telescope shots can be assumed. TANDEM imagery always consists of a set of four .fits frames, one for each telescope. After preview, the whole set can be totally or partially stored on local hard disk drive via the USB 3.0 transfer protocol, carrying the appropriate information on individual pointing coordinates, filter setup, and exposure details in the .fits header. Just after the download, in about 1 s, the system is ready for a new series of images.

In case a quick and/or repeated battery of observations is required (like for instance for SST applications) the software interface can automatically operate each of the four telescopes one at a time by executing a batch of instructions from a coded text file.

3.4. First Observing Feedback

A general emerging trend in digital technology is that CMOS detectors are getting more and more popular in the astronomical domain, overcoming the established CCD technology that ruled over the last few decades. CMOS chips allow a fully electronic management of the acquisition process, including exquisite control over the exposure time down to very short (∼10 ms or so) timescales, overriding any mechanical shutter. Cooling constraints are less severe than for CCDs, usually requiring cheaper Peltier electronics for temperature control, while sporting quantum efficiency factors fully comparable with cooled CCDs.

On the other hand, warmer operating conditions make CMOS imagery much more prone to electronic noise disturbance with increasing exposure time, a feature that usually limits the dynamical range of the image and the maximum exposure time for the chip to saturate, usually set to a few minutes at most. Compared to CCDs, these special characteristics require a change in the CMOS observing strategies, avoiding large one-shot exposures and better relying on postprocessing procedures of stacking and composition of original series of short-exposure frames.

3.4.1. Photometric Characterization

In order to characterize the GSense 4040 throughput in the different Johnson–Cousins photometric bands, we carried out a number of observing tests with the TANDEM telescopes on A. U. Landolt (1992) stellar calibration fields, in order to assess the magnitude limit and the saturation threshold with varying the exposure time. The photometric zero-points (ZPs) in the different bands are a key parameters, in this regard, to set the magnitude scale, as

$$\mathrm{mag} = -2.5\log\left[\frac{c(t)}{t}\right] + \mathrm{ZP}]. \tag{11}$$

In the equation, $c(t)$ is the ADU signal counts collected during an exposure of t seconds. The four telescopes performed very similarly so that, after the standard reduction procedure, on average, the resulting ZPs for the Johnson–Cousins photometric system are as in the second column of Table 2.

As a 16 bit digital depth is used by the GSense 4040 electronics for image display, then a maximum signal count of $c_{\max} = 2^{16} = 65{,}536$ can be sampled by the detector,[6] and for each telescope a saturation threshold easily derives as

$$\begin{aligned}\mathrm{mag_{sat}} &= -2.5\log\left(\frac{65536}{t}\right) + \mathrm{ZP}\\ &= 2.5\log(t) + (\mathrm{ZP} - 12.04).\end{aligned} \tag{12}$$

The saturation magnitude for a 1 s exposure in the different bands[7] is reported in the third column of Table 2. A more elaborate analysis is needed, on the contrary, for a suitable assessment of the magnitude limit that can be reached by the TANDEM telescopes. The detection threshold is, in fact, of statistical nature and it therefore depends on the assumed signal-to-noise ratio (S/N) of the target detection and the exposure time. In addition, sky brightness and seeing conditions may play a role.[8] The problem has been discussed in A. Buzzoni (2024b), and a more extensive treatment has been proposed in A. Buzzoni et al. (2016, see in particular Equation (6) therein). A general dependence for the magnitude limit may eventually be envisaged in the form

$$\begin{aligned} m_{\lim} &= \mathrm{ml} + 1.25\log\left(\frac{t}{1000}\right)\\ &\quad - 2.5\log\left(\frac{\mathrm{S/N}}{3}\right) + 0.5(\mathrm{SB} - \mathrm{sbl}),\end{aligned} \tag{13}$$

by taking as a reference case a detection threshold at $\mathrm{S/N} = 3$ with an exposure time of 1000 s and the typical figures for the Loiano sky brightness (sbl) to be expressed in units of mag arcsec^{-2} (see, in this regard, V. Zitelli 2000). The calibration on the A. U. Landolt (1992) standard fields provided the following set of parameters in Equation (13), as summarized in Table 2.

Table 2
The Photometric Zero-points, and Detection and Saturation Thresholds for TANDEM's Individual Telescopes, as from Equations (11)–(13)

Filter	ZP (mag)	Saturation mag @1 s (mag$_{\rm sat}$)	Mag Limit @1000 s (ml)	Loiano Sky Brightness (sbl)
B	21.11 ± 0.11	9.1	19.6	20.7
V	20.88 ± 0.04	8.8	19.2	19.9
R_c	21.19 ± 0.03	9.2	19.3	19.6
I_c	20.49 ± 0.05	8.5	18.4	18.4

An illustrative summary of the magnitude limit at an $\mathrm{S/N} = 3$ detection level from the Loiano skies (i.e., sky brightness, SB = sbl), and the saturation magnitude versus exposure time for the different photometric bands is displayed in Figure 14. Clearly, $2.5\log(\sqrt{4}) = 0.75$ fainter magnitudes can be reached for the same exposure time and S/N threshold when combining the four TANDEM telescopes in the "collimated" configuration, as in Figure 11.

As a relevant feature, note from the plot that the CMOS dynamical range (that is, the difference between saturation magnitude and magnitude limit) drastically shrinks with increasing exposure time as the CMOS saturation scales with $1/t$ while the detection threshold scales with $1/\sqrt{t}$. As we have been discussing before, this explains why stacked short-exposure frames have to be preferred to one-shot large exposures, all the way.

3.4.2. Astrometric Characterization

The astrometric performance of TANDEM's telescopes has been assessed by relying on the recognized software Astrometrica[9] (H. Raab 2012) for plate-solving procedures. This software is extensively used for SSA applications, specially dealing with near-Earth asteroid follow-up. Astrometrica's solving core was matched with the recent Gaia Data Release 2 (DR2) star catalog (L. Lindegren et al. 2018), which provides the most accurate reference grid available for astrometry (see,

6 An excellent linearity in the GSense 4040 detector response up to about 60,000 ADU was actually verified along the operational tests.

7 Namely, the quantity (ZP − 12.04) in Equation (12). Note, by the way, that the saturation magnitude is in fact an indicative figure for a 1 pixel point source. Brighter objects could still be correctly imaged, of course, if their signal spreads across many pixels.

8 Given the PS of the TANDEM telescopes, the seeing dependence is not an issue for our case and we will not consider it here.

9 Available at http://www.astrometrica.at.

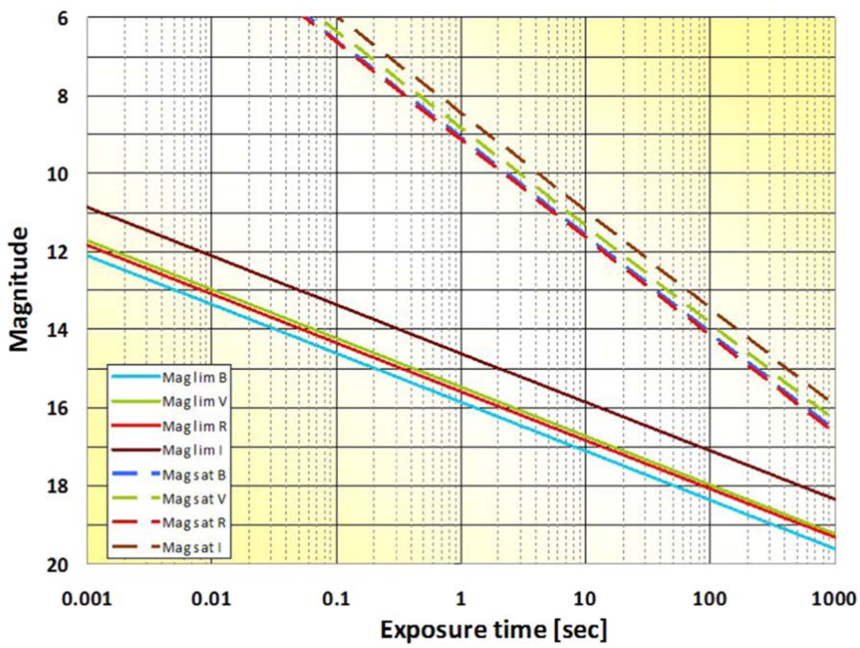

Figure 14. According to Equation (13), solid lines display the magnitude limit for an S/N = 3 detection threshold in the different photometric bands (as reported in the legend on the plot) reached by each TANDEM telescope with increasing exposure time. The corresponding saturation cap is also showed (dashed lines) according to Equation (12).

e.g., A. Buzzoni 2024a, for a comparative discussion on this subject).

The A. U. Landolt (1992) dense star field around PG1528 +062 was taken for our standard tests. Images with the four TANDEM telescopes were compared with the star catalog sources to derive the plate solution. As expected, due to residual optical aberrations at the extreme edges of the FOV, astrometric accuracy slightly degrades radially from the image center, still securing, however, an outstanding performance with mean residuals well within 0.20″ (that is about one-tenth of a pixel) in the central region of the frame, as shown in Figure 15.

As a further and more challenging test, recent observations of the two near-Earth asteroids 2011 UL21 and 2024 MK during their Earth close encounter of 2024 June led to even more outstanding figures for TANDEM's astrometry, with orbit residuals for the two objects of 0.08″–0.09″ in R.A. and 0.04″–0.05″ in decl. (A. Carbognani 2024a, 2024b).

4. Results and Discussion

Wide-field telescopes with a large collecting area are the elected instruments for a broad range of astronomical applications, including deep-sky surveys and quick-alert optical recognition of sky transients (e.g., supernovae, GWs, and GRB events). A strategic role of these telescopes may also be envisaged for any SSA application, sensing the solar system environment for (potentially threatening) small bodies (asteroids and comets), and the anthropic traffic of artificial satellites and space debris in the circumterrestrial surroundings.

Though so different, both the galactic/extragalactic and SSA contexts rely in fact on the same strategy as observers ideally aim at detecting objects as faint as possible over an FOV as wide as possible. A large collecting area (to reach fainter apparent magnitudes) and focal length as short as possible (to inspect a larger portion of the sky at one time) are mandatory for our telescope, thus calling for a "fast" optical design (that is a small f/number) all the way.

However, according to A. Buzzoni (2024b), special caution should be exercised on the following relevant points.

1. In general, the telescope focal length (F), expressed in meters, leads to a PS of the order of PS $\approx (2.1/F)(px_\mu/10)$ arcsec pixel^{-1} (e.g., A. Buzzoni 2024a) on a CMOS/CCD detector, by expressing the pixel size (px_μ) in units of μm. As pixel sizes of 5–10 μm are currently typical, normally the atmospheric seeing figure (FWHM) tends to be severely undersampled across the image.
2. For any ground-based telescope, both seeing and pixel scale always largely exceed the diffraction limit of the instrument, as constrained by the Airy disk. This eventually makes the resolving power of our telescope basically seeing (and/or pixel) limited.
3. Petzval field curvature is always present, together with astigmatism and coma aberrations, when observing with "fast" telescopes with a short focal length (e.g., D. J. Schroeder 1987). If not suitably corrected, this causes the image quality to drastically degrade at the edges of the FOV.

As a consequence, target "morphology" may hardly be a main focus of our investigation when dealing with any wide-field observational context, as detection efficiency and integrated aperture photometry usually suffice for our target inventory, especially if reasons exist to expect targets of point-source nature.

For this reason, we have shown in Section 2 that a convenient "synthetic" proxy to any big monolithic telescope can be obtained in terms of an array of smaller (independent) instruments. If a set of N (identical) telescopes are assembled, each with aperture $d_{\rm array}$ and f/number $f_{\rm array}$, then a "faster" synthetic aperture $D_{\rm mono} = \sqrt{N}\, d_{\rm array}$ and $f_{\rm mono} = f_{\rm array}/\sqrt{N}$ can be obtained. Once considering the A. Buzzoni (2024b) cost

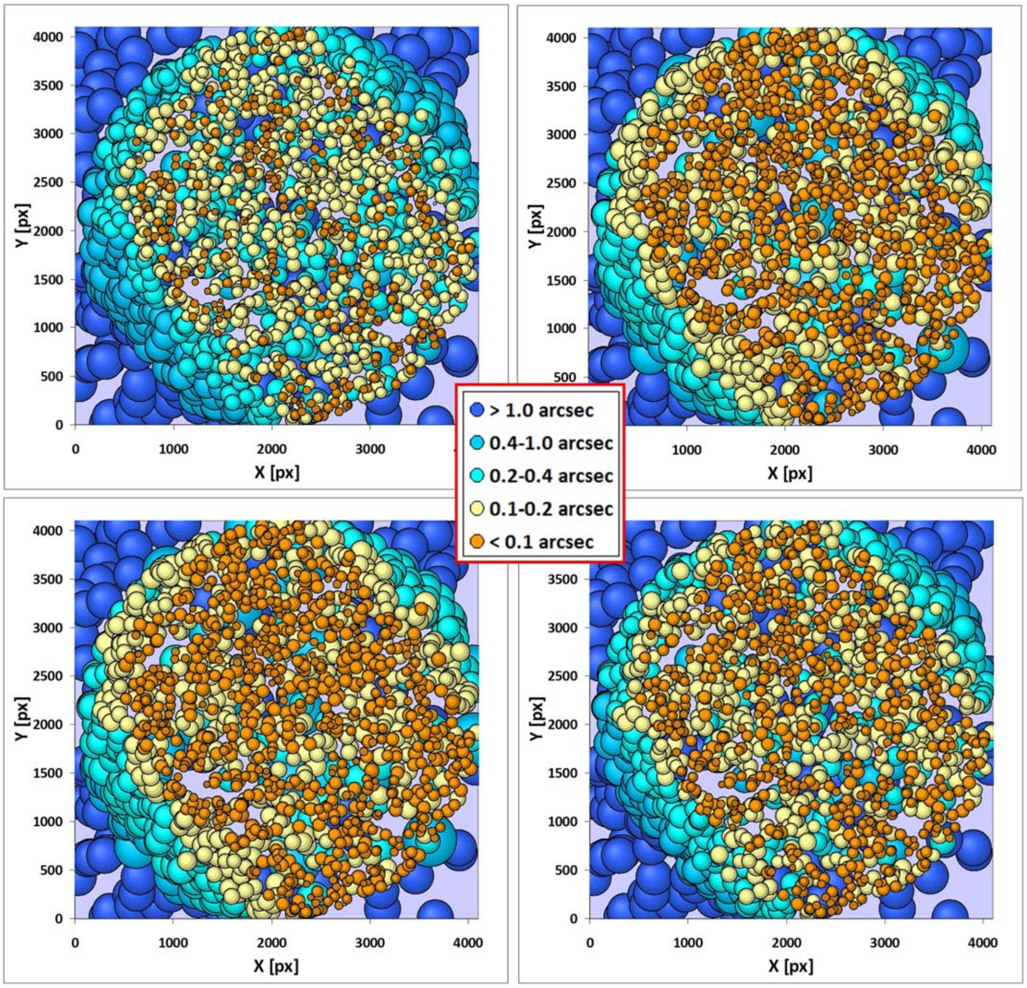

Figure 15. Astrometric accuracy of the four TANDEM telescopes (coded with T1, T2, T3, and T4 in the plots) across a $2^\circ \times 2^\circ$ dense stellar field around the A. U. Landolt (1992) standard PG1528+062. Each panel maps the 4096×4096 pixel GSense 4040 image. Plate solutions were obtained independently for each telescope by relying on the Astrometrica + Gaia DR2 catalog, as a reference. Star size in the plots is proportional to the astrometric uncertainty. As summarized in the central legend inset, orange dots are stars with an astrometric accuracy of $0.1''$ or better, yellow dots are for $0.1''$–$0.2''$, cyan dots are for the $0.2''$–$0.4''$ range, pale blue dots are for $0.4''$–$1.''0$ residuals, and finally dark blue dots are for stars displaying astrometric residuals in excess of $1''$.

model, summarized in Equation (1), then a cost-effective solution can be reached for the combination, compared to an equivalent $(D, f)_{\rm mono}$ monolithic case.

All these arguments set the background for the TANDEM project (see Figure 2), to equip the INAF-OAS observatory in Loiano, Italy, with a cost-effective wide-field telescope exploiting the telescope-array concept. To a large extent, TANDEM pushes forward a fully innovative concept, where a maximum flexibility is achieved between individual maneuvering of each of the four 35 cm $f/3$ Newtonian telescopes and the "collimated" observing configuration, which synthesizes a 70 cm $f/1.5$ monolithic telescope with a 4 deg^2 FOV.

As described in Section 3.3, a trade-off between angular and sensitivity performances is allowed by the system, as the observer can either use TANDEM at its deepest magnitude sensitivity by converging the four telescopes on the same $2^\circ \times 2^\circ$ FOV or, alternatively, fully exploit the wider angular coverage on sky by steering each telescope in a different direction such as to simultaneously mosaic four (adjacent or sparse) fields, up to 20° apart, for up to 16 deg^2.

Given the wide FOV allowed by the "fast" optical design, special care had to be devoted to an accurate correction of optical aberrations for the TANDEM telescopes. As we discussed in Section 3.2.2, for this task we designed an optimized field corrector based on a C. G. Wynne (1974) classical achromatic triplet.

TANDEM imagery is provided by a set of four Moravian C4-16000 cameras each carrying a motorized and remotely controlled filter wheel to reproduce the Johnson–Cousins BVR_cI_c standard system (see Figure 5). CMOS technology is adopted on board thanks to a front-illuminated Grade 1 GSense 4040 (4096×4096 pixels) monochrome chip with a 9 μm pixel size (projecting an angular scale of $1.''75$ pixel^{-1}) and an electronic shutter. The latter allows exposure to be handled electronically on extreme timescales of just 0.02 ms (see Figure 3), which is also the readout lapse per pixel row.

As chip readout proceeds sequentially by rows, then a small (yet recoverable) drift, in the order of few 10^{-2} s, may be introduced in the nominal time tag of the shot. While fully negligible for any standard astronomical application, the so-called "rolling shutter" effect, a recognized feature of CMOS technology (see, e.g., C. Liang et al. 2008), should be carefully considered, however, in case of accurate time tag as in SST observations.

Under Loiano's typical sky conditions, the observing feedback based on A. U. Landolt (1992) calibration fields

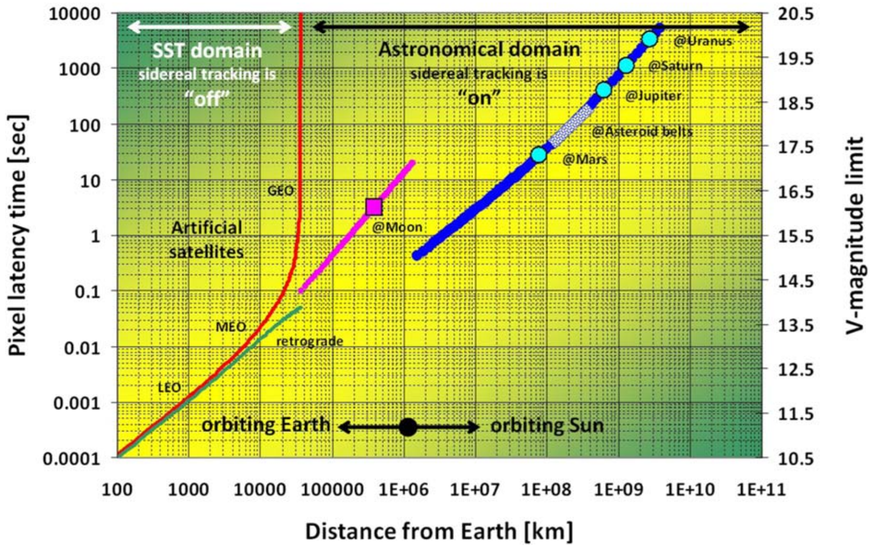

Figure 16. Pixel latency time (in seconds, left scale) across the TANDEM CMOS detector for objects in motion according to different dynamical environments. Latency time directly reflects into a magnitude threshold for object detection (right scale), through Equation (13). In particular, the SST domain includes Earth-orbiting artificial satellites and space debris (both in prograde and retrograde motion, respectively, red and green coded in the plot) at the different orbital regimes, namely low-, medium-Earth, and geostationary orbits (see, e.g., B. Pattan 1993, for details), up to the circumterrestrial outer edge at about 35,786 km. Due to their special nature, SST observations are typically carried out with telescope sidereal tracking "off" (see A. Buzzoni 2024a, for further insights upon SST observing strategies). Magnitude threshold for deep-space objects, at the Moon distance and beyond, as marked, is accounted for by the magenta curve. Detection limits for even farther solar system objects, at increasing planetary distance, are finally accounted for by the blue curve, which also includes the illustrative TANDEM detection threshold for main-belt asteroids. These observations usually require a more standard astronomical approach, with sidereal tracking "on," as labeled on the plot.

allowed us to estimate that a magnitude of $V_{\rm lim} \sim 19$ can be reached by TANDEM's individual telescopes in 15 minute exposures for stars at an $S/N = 3$ detection threshold (see Figure 14). A 0.75 mag deeper limit can be reached, of course, in the "collimated" configuration of the combination, by fully exploiting the 70 cm synthetic aperture of the equivalent monolithic telescope.

This standard assessment appropriately applies, of course, to any classical astronomical context, where sidereal telescope tracking enables, in principle, large integrations on fixed (stellar or extragalactic) targets. This may not be the case, however, for a more broad range of application of the TANDEM system, especially aimed at characterizing celestial objects in (fast) motion across the sky.

As extensively discussed in A. Buzzoni (2024a), what really sets a telescope's sensitivity in the latter case is the pixel latency time ($\tau_{\rm px}$), which is the lapse a moving object spends over the same pixel of the CMOS/CCD detector, depending on the apparent motion angular rate. In fact, any longer exposure, in excess to $\tau_{\rm px}$, does not add to the target detection, as the signal is diluted over several pixels, while the noisy background keeps increasing with time. As a consequence, for any exposure longer than $\tau_{\rm px}$, our target detection degrades as $S/N(t) \propto 1/\sqrt{t}$ (see, e.g., Equation (13) in A. Buzzoni 2024a). Providing to maintain the exposure within the pixel latency time, the TANDEM effective magnitude limit in the different motion regimes for objects in orbit around Earth and around the Sun can be assessed with the help of Figure 16, by introducing the pertinent value of $\tau_{\rm px}$ in Equation (13). Note, from the figure, that extremely short exposures (10^{-2}–10^{-3} s) are suitable for SST applications, a feature that evidently takes advantage of the unique performance of TANDEM, thanks to its CMOS technology.

By means of the Astrometrica software package we also investigated TANDEM's astrometric performance on A. U. Landolt's (1992) stellar fields to homogeneously probe the whole FOV. For all telescopes, plate-solving procedures consistently point to an inherent angular accuracy of some $0\rlap{.}'1$–$0\rlap{.}'2$ (or about one-tenth of a pixel), at least in the central region of the frame (see Figure 15).

While especially conceived for SST activities, in the framework of the European Consortium for Space Surveillance and Tracking, TANDEM may find useful applications also in a more direct astronomical context. According to previous arguments, among the many envisaged fields of research, which could usefully take advantage of TANDEM's special capabilities, the following cutting-edge science cases (a not necessarily exhaustive list) could be mentioned for their relevance.

1. Search for optical counterparts of supernovae, GRB, GW, and fast radio burst events.
2. Search for exoplanets with the transit method (W. J. Borucki & A. L. Summers 1984).
3. Search for main-belt, NEO, Atira (A. O. Ribeiro et al. 2016), and other potentially hazardous asteroids.
4. Search for interstellar intruders (comets and asteroids like 1I/'Oumuamua, M. Micheli et al. 2018b; or 2I/Borisov, P. Guzik et al. 2020).
5. Study of meteoric impacts on the Moon (e.g., J. M. Madiedo et al. 2015).
6. Study of stellar streams in the Galaxy (and other archeoastronomy applications; see, e.g., V. Belokurov et al. 2006).
7. Wide-field survey of extragalactic star clusters and variable stars in Local Group galaxies.
8. Study of any serendipitous celestial transient.

Acknowledgments

It is a pleasure to acknowledge the referee for their kind and inspiring report, which helped improve the final version of the paper.

The research activities and technological achievements described in this paper have received funding from the European Commission Framework Programme "Space Surveillance and Tracking" contract Horizon 2020 research and innovation program, under grant agreement No. 952852, and the EU Space Programme under grant EUSST2023-26GA.

Appendix

For the reader's convenience, according to the previous discussion, we report here in Table A1 a synoptic summary of the Cassini + TANDEM system.

Table A1
A Synoptic Comparison of the Cassini + TANDEM Optical System

Configuration	TANDEM $1 \times T$	TANDEM $4 \times T$	Cassini BFOSC
Primary mirror (mm)	350	700	1520
Mirror design	Parabolic	…	Ritchey–Chrétien
Optical design	Newtonian +4″ Wynne corrector 1×		Cassegrain …
Secondary mirror (mm)	140 (flat)	…	580 (hyperbolic)
f/# @prime focus	$f/3.0$	$f/1.5$	$f/3.0$
f/# @Cassegrain focus	…	…	$f/8.0$
f/# @detector	$f/3.0$	$f/1.5$	$f/4.64$
Camera	Moravian C4-16000		Princeton Instruments VersArray1300B-LN
Detector and image characteristics			
Detector	GSense 4040 CMOS		EEV CCD 36-40
Front/back illuminated	Front illuminated		Back illuminated
Image dynamical range	16 bits		16 bits
DQE @5000 Å	70%		80%
Cooling	One-stage Peltier		Liquid N_2 @$T = -110$ °C
	thermoelectric module		…
	~30 °C below ambient		…
Readout noise (rms)	3.9 e^-		3.1 e^-
Shutter	electronic		mechanical
Minimum exposure time	21 μs		0.1 s
Number of pixels	4096 × 4096		1340 × 1300
Pixel size	9 μm		20 μm
Pixel angular scale	1′.75		0′.58
FOV	2° × 2°	up to 16 deg^2	13′×12′.6
Mag limit in 1000 s	19.3	20.1	21.6
@S/N ~ 3 (R band)	…	…	…

ORCID iDs

A. Buzzoni https://orcid.org/0000-0002-6514-1870
A. Carbognani https://orcid.org/0000-0002-0737-7068
E. Diolaiti https://orcid.org/0000-0002-3978-0695
G. M. Stirpe https://orcid.org/0000-0002-3702-8731
F. Bonoli https://orcid.org/0000-0001-8611-5009
I. Bruni https://orcid.org/0000-0002-1560-4590
F. Cortecchia https://orcid.org/0000-0001-5072-7791
I. Foppiani https://orcid.org/0000-0001-8014-2233
S. Galleti https://orcid.org/0000-0003-3825-2273
M. Lombini https://orcid.org/0000-0001-9818-9283
L. Schreiber https://orcid.org/0000-0002-6657-8054

References

Abraham, R. G., & van Dokkum, P. G. 2014, PASP, 126, 55
Alessi, E. M., Buzzoni, A., Daquin, J., Carbognani, A., & Tommei, G. 2021, AcAau, 179, 659
Belokurov, V., Zucker, D. B., Evans, N. W., et al. 2006, ApJL, 642, L137
Blake, J. 2022, A&G, 63, 2.14
Borucki, W. J., & Summers, A. L. 1984, Icar, 58, 121
Burke, B., Jorden, P., & Vu, P. 2005, ExA, 19, 69
Buzzoni, A. 2024a, AdSpR, 74, 4990
Buzzoni, A. 2024b, RASTI, submitted
Buzzoni, A., Altavilla, G., Fan, S., et al. 2019a, AdSpR, 63, 371
Buzzoni, A., Altavilla, G., & Galleti, S. 2016, AdSpR, 57, 1515
Buzzoni, A., Guichard, J., Altavilla, G., et al. 2019b, in First Int. Orbital Debris Conf., Vol. 2109 (Houston, TX: LPI), 6067
Carbognani, A. 2024a, Minor Planet Circular Supplements, MPS_20240708, 2193869, https://www.minorplanetcenter.net/iau/ECS/MPCArchive/2024/MPS_20240708.pdf
Carbognani, A. 2024b, Minor Planet Circular Supplements, MPS_20240708, 2199970, https://www.minorplanetcenter.net/iau/ECS/MPCArchive/2024/MPS_20240708.pdf
Carbognani, A., & Buzzoni, A. 2020, MNRAS, 493, 70
Carbognani, A., Buzzoni, A., & Stirpe, G. 2021, MNRAS, 506, 5774
Cousins, A. W. J. 1976, MmRAS, 81, 25
Daquin, J., Alessi, E. M., O'Leary, J., Lemaitre, A., & Buzzoni, A. 2021, NonDy, 105, 2081
Di Cecco, A., Buzzoni, A., Mochi, M., et al. 2023, in II NEO and Debris Detection Conf. (Noordwijk: ESA), 64
Dorißen, J., Rojacher, C., Grunwald, T., Schmitt, R. H., & Bergs, T. 2022, Procedia CIRP, 111, 827
Fulle, M., Lazzarin, M., La Forgia, F., et al. 2022, MNRAS, 513, 5377
Furenlid, I. 1984, AASPB, 36, 5
Guzik, P., Drahus, M., Rusek, K., et al. 2020, NatAs, 4, 53
Hainaut, O. R., & Williams, A. P. 2020, A&A, 636, A121
Hoffleit, D., & Warren, W. H. 1987, ADCBu, 1, 285
Hoffman, A., Loose, M., & Suntharalingam, V. 2005, ExA, 19, 111
Ivezić, Ž., Kahn, S. M., Tyson, J. A., et al. 2019, ApJ, 873, 111
Johnson, H. L. 1966, ARA&A, 4, 193
Karpov, S., Bajat, A., Christov, A., et al. 2020, Proc. SPIE, 11454, 114540G
Landolt, A. U. 1992, AJ, 104, 340
Lawler, S. M., Boley, A. C., & Rein, H. 2022, AJ, 163, 21
Lawrence, A., Rawls, M. L., Jah, M., et al. 2022, NatAs, 6, 428
Liang, C., Peng, Y., & Chen, H. 2008, ITIP, 17, 1323
Lindegren, L., Hernández, J., Bombrun, A., et al. 2018, A&A, 616, A2
Madiedo, J. M., Ortiz, J. L., Organero, F., et al. 2015, A&A, 577, A118
Mariappan, A., & Crassidis, J. L. 2023, FrST, 4, 1309940
Micheli, M., Buzzoni, A., Koschny, D., et al. 2018a, Icar, 304, 4
Micheli, M., Farnocchia, D., Meech, K. J., et al. 2018b, Natur, 559, 223
Pattan, B. 1993, Satellite Systems: Principles and Technologies (New York: Springer)
Raab, H. 2012, Astrometrica: Astrometric data reduction of CCD images, Astrophysics Source Code Library, ascl:1203.012
Ribeiro, A. O., Roig, F., De Prá, M. N., Carvano, J. M., & DeSouza, S. R. 2016, MNRAS, 458, 4471
Roddier, F. 1981, PrOpt, 19, 281
Schroeder, D. J. 1987, Astronomical Optics (San Diego, CA: Academic Press), 363
Tyson, J. A. 2002, Proc. SPIE, 4836, 10
Waltham, N. 2010, ISSIR, 9, 391
Wynne, C. G. 1972a, MNRAS, 160, 13P
Wynne, C. G. 1972b, PrOpt, 10, 139
Wynne, C. G. 1974, MNRAS, 167, 189
Zitelli, V. 2000, MmSAI, 71, 193